PAPER
Hongjun You, Jixiang Fang *et al.*
Hierarchical silver mesoparticles with tunable surface topographies for highly sensitive surface-enhanced Raman spectroscopy

PAPER

Hierarchical silver mesoparticles with tunable surface topographies for highly sensitive surface-enhanced Raman spectroscopy†

Lin Cheng,[a] Chuansheng Ma,[b] Guang Yang,[b] Hongjun You*[a] and Jixiang Fang*[a]

Using a simple aqueous synthesis method, Ag hierarchical mesoparticles with tunable surface topography were obtained. The mechanism of tuning the topographies of the hierarchical mesoparticles in this particle-mediated anisotropic growth system was studied. A series of Ag mesoparticles with well-tuned surface topographies were synthesized as an ideal research target for a systematic investigation of the effect of surface nanostructures on the performance of surface enhanced Raman spectroscopy (SERS). Highly-branched Ag mesoparticles were shown to have the highest SERS sensitivity both as single-particle SERS substrates and particle-array SERS substrates, which have an enhancement factor greater than 10^9. Using the finite difference time domain method, the distribution of the localized electromagnetic field near the particle surface was simulated. Based on the simulation results, the mechanism of the effect of topography on the SERS properties was systematically studied.

Introduction

Surface-enhanced Raman scattering (SERS) involves the amplification of Raman signals by several orders of magnitude, this is mainly attributed to the collective oscillations of the conduction electrons through the electromagnetic interaction of light with metals, known as surface plasmon resonance (SPR).[1–3] Recently, SERS as a powerful analytical tool has been shown to have wide potential applications in biochemistry, chemical production, food safety and environmental monitoring.[4–8] The sensitivity of SERS depends highly on the surface topography of the substrate.[9,10] The interstitial sites, nanoscaled cavities, and bifurcations constructed on the SERS substrate can produce a plasmonic coupling effect which can lead to local surface plasmon resonance (LSPR). The LSPR makes a great contribution to the enhancement of SERS.[11,12]

Up to now, various kinds of SERS substrates have been synthesized. In general, the SERS substrates, possessing a rough surface, can be classified into three main classes: metallic electrodes, periodic nanostructures, and metallic nanostructured particles.[12] The metallic electrode substrates are prepared through electrochemical deposition, and were initially used to study the SERS phenomenon, this has had a great effect on the

development of SERS.[13,14] However, because of the relatively low enhancement factors (EFs) and reproducibility, these substrates have been replaced by periodic nanostructures for practical applications. Periodic nanoconstructed substrates have been prepared by advanced "top-down" nanopatterning techniques, such as electron beam lithography,[15] nanoimprinting,[16] molecular beam epitaxy,[17] and template-based methods using polystyrene spheres.[18] Using these techniques, it is possible to attain regular, uniform and periodic two-dimensional patterns.[19–21] Nevertheless, it is still difficult to achieve complex three-dimensional nanoscale structures by means of the current "top-down" techniques. Recently, metallic nanostructured particles have attracted great interest as SERS substrates due to the fact that fine nanoscale structures can be constructed on a particle surface using "bottom-up" chemical synthesis methods. For example, narrow nanogaps down to a size of 1 nm have been formed on Au and Ag particles, these had EF greater than 10^8 for single-particle SERS.[22,23] These metallic particles with nanotextured surface topographies can not only be used as single-particle SERS substrates but can also be aggregated to form particle-array SERS substrates.[24] As single-particle SERS substrates, these particles can be dispersed in solution or delivered into cells through the blood flow to detect the Raman signals of molecules located in solutions or cells.[25–27] As particle-array SERS substrates, the interparticle interactions in the array can produce additional and/or more abundant "hot spots" for SERS.[28,29]

Up to now, some Ag or Au particles with various nanotextured surface topographies have been synthesized and studied as SERS substrates, such as meatball-like,[9] star-like,[30] sea urchin-like,[12] flower-like,[31] and highly-branched mesoparticles.[32] The nanostructured protrusions on these hierarchical particles serving as

aState Key Laboratory for Mechanical Behavior of Materials, School of Science, Xi'an Jiaotong University, Shaanxi, 710049, P. R. China. E-mail: hjyou@mail.xjtu.edu.cn; jxfang@mail.xjtu.edu.cn

bKey Laboratory of the Ministry of Education and International Center for Dielectric Research, Xi'an Jiaotong University, Shaanxi, 710049, P. R. China

† Electronic supplementary information (ESI) available: EDX analysis and calculation of SERS EFs. See DOI: 10.1039/c3ta14674j

nano-lightning rods, dramatically increase the electromagnetic field in the vicinity of the tips, and thus generate plenty of enhanced SERS "hot spots" on the surface of the particles.[33–35] The surface topographies have an important effect on the optical and SERS properties. Although these hierarchical mesoparticles with various nanotextured topographies have been separately synthesized and studied as SERS substrates, the systematic investigation of the effect of topographies on the SERS properties is still rather limited. In this paper, a series of Ag mesoparticles with well controlled surface morphologies have been obtained using a very simple synthesis system. Using both experimental measurements and theoretical calculations, the mechanism of the effect of topography on SERS activities was systematically studied.

Experimental section

Materials

Silver nitrate (AgNO$_3$, 99%) and L-ascorbic acid (L-AA, 99%) were purchased from Sigma Aldrich. Deionized water (Millipore) with a resistance of 18.2 MΩ was used. The L-AA solutions used in all the experiment were freshly prepared.

Synthesis of Ag mesoparticles

In a typical synthesis, 0.05 mL of 100 mM AgNO$_3$ aqueous solution and 7.45 mL water were mixed in a glass vial. Then 2.5 mL of 200 mM L-AA aqueous solution was added immediately. The reaction was conducted at room temperature with a 200 rpm rotating magnetic bar (the length of the magnetic bar was 3 cm). The colour of the reaction solution changed from colourless to light grey. After 10 min, the as-synthesized product was centrifuged at 4500 rpm (the length of the rotor was 10 cm, so the linear rate of the rotation was 47 m s^{-1}) for 2 min and then washed several times with alcohol and water for further characterization. In all the experimental syntheses of the silver particles the total volume of the reaction was fixed at 10 mL and the experimental conditions (concentration of the reagents, reaction time, and stirring rate) were changed.

Characterization

The morphology of the samples was characterized using field-emission scanning electron microscopy (SEM) (JEOL JSM-7000F) at an accelerating voltage of 20 kV and transmission electron microscopy (TEM) (JEOL JEM-2100) at an accelerating voltage of 200 kV. The Raman spectrum measurements were carried out on a confocal microprobe Raman spectrometer (LabRAM HR800, HORIBA JOBIN YVON) with a 633 nm He–Ne laser line at room temperature. The signal collection time was 1 s for the detection of particles aggregation and 20 s for single-particle detection with a laser spot of 850 nm diameter. The sample for SERS measurement was prepared by dropping some of the silver particles dispersion on a clean silicon wafer (7 mm × 7 mm). After drying, 100 μL of 1 × 10^{-7} M aqueous crystal violet (CV) solution was dropped on it (keep lucifugal during drying).

Finite difference time domain simulation

Based on the SERS samples in Fig. 7, five models were built and their geometric structures were designated as an approximate treatment. The details of the five models are described in the ESI.† The three-dimensional finite difference time domain (FDTD) simulation was used to calculate the electric field distribution and the electromagnetic enhancement under the excitation light with wavelengths of 514 nm, 633 nm and 785 nm. The incident light was in the form of plane waves which propagated along the z-axis backward and polarized along the x-axis. It was assumed that each geometrical model was suspended in air ($n_0 =$ 1.0). The frequency (ω) dispersive and complex dielectric function for Ag, ε_{Ag} (ω), was obtained from the Handbook of Optical Materials. The grid size was 4 nm for the space deviation.

Results and discussion

Topography tuning of hierarchical silver mesoparticles

In a simple aqueous solution synthesis system, containing only two reagents, AgNO$_3$ and L-AA, a series of hierarchical Ag mesoparticles were obtained. By changing the experimental conditions, such as concentrations of AgNO$_3$ and L-AA, rotation rate, and reaction times, the topography of the silver mesoparticles could be well controlled and tuned. As shown in Fig. 1, the topographies of the obtained Ag mesoparticles were successfully tuned from meatball-like shapes (Fig. 1a and b) to coral-like (Fig. 1c and d), urchin-like (Fig. 1e), and highly-branched shapes (Fig. 1f). All kinds of hierarchical Ag mesoparticles were found to be uniform in morphology and size. The meatball-like mesoparticles were around 720 nm and 950 nm in diameter, separately in samples S1 and S2, and were constructed by the aggregation of nanoparticle units which were a small size in S1 and large in S2. From S3 to S5, the bulges on the surface became dense accompanied by an increase in their length and a decrease in their diameter. The particle sizes of S3 to S5 changed from about 1 to 2 μm. For sample S6, the density of the branches reached a maximum and the second sub-branches grew over the main branches. The size of the total particles increased to about 1.6 μm.

The synthesis conditions for these Ag mesoparticles are listed in ESI (Table S1†). Compared with the reaction time and rate of rotation of the magnetic bar, the concentrations of AgNO$_3$ and L-AA have a more important effect on the morphology. When the concentration of AgNO$_3$ was kept at 1 mM, and the concentration of L-AA was changed from 0.5 to 10 and 20 mM, the morphologies of the Ag mesoparticles changed from meatball-like shapes (sample S1 and S2) to urchin-like shapes (sample S5). When the concentration of L-AA was kept at 10 mM, and the concentration of AgNO$_3$ was decreased from 1 mM (sample S2) to 0.5 mM (sample S4), the bulge on the surface of the particles became longer and thinner. Therefore, both an increase of L-AA concentration and a decrease of AgNO$_3$ concentration could improve the protuberated growth.[36] When the concentration of AgNO$_3$ was decreased to 0.5 mM and the concentration of L-AA was increased to 50 mM, the greatly protuberated anisotropic growth induced a highly-branched morphology (sample S6). From a comparison of samples S3 and S4, the reaction time and rate of rotation of the magnetic bar were also found to have an effect on the morphology.

The morphology of the Ag mesoparticles was tuned not only in a wide scope, such as from meatball-like to highly-branched
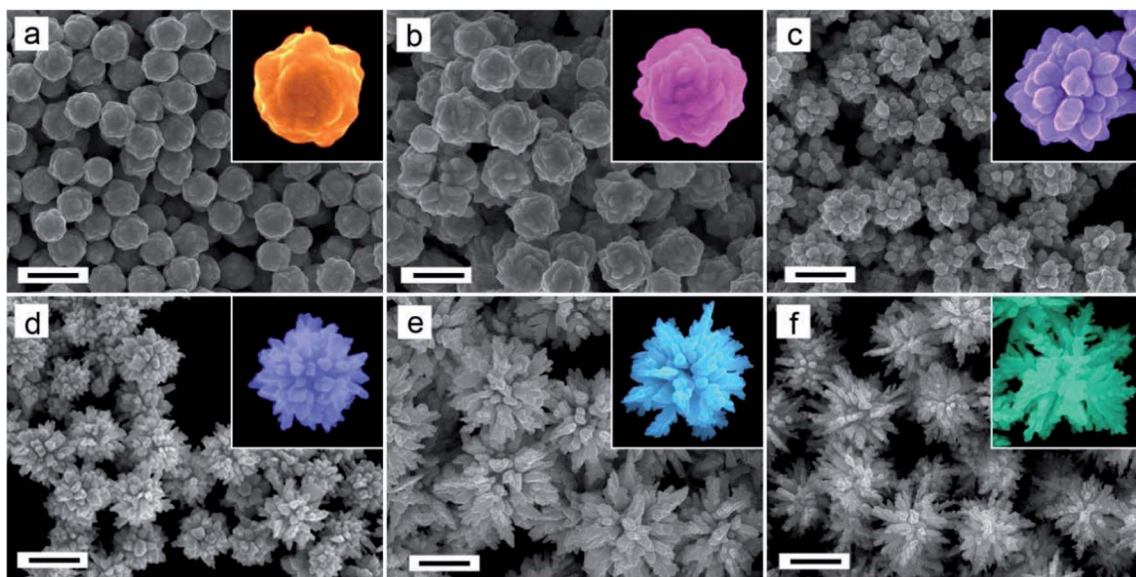
Fig. 1 SEM images of Ag mesoparticles with tunable surface topographies produced by changing the synthesis parameters. The concentration of AgNO$_3$ was 1 mM for samples (a) S1, (b) S2, and (e) S5, and 0.5 mM for samples (c) S3, (d) S4, and (f) S6. The concentration of L-AA was 0.5 mM for S1, 10 mM for S2, S3, and S4, 20 mM for S5, and 50 mM for S6. The reaction time was 20 min for S1, S2, and S5, 15 min for S3, and 10 min for S4 and S6. The rate of rotation of the magnetic bar was 130 rpm for S1, S2, S4 and S5, 150 rpm for S3, and 200 rpm for S6. The scale bars represent 1 µm.

shapes, but could also be continuously fine-tuned. As is shown in Fig. 2, by slightly changing the concentration of AgNO$_3$ and L-AA, a series of coral-like Ag mesoparticles were obtained. When 0.25 mM AgNO$_3$ and 0.5 mM L-AA were used, a coral-like structure with relatively few main and subordinate branches was produced (Fig. 2a). Keeping the concentration ratio constant and changing their concentrations to 0.5 mM and 1 mM, the Ag

coral-like structure produced had more main branches and subordinate branches (Fig. 2b). If we used 0.25 mM AgNO$_3$ and 10 mM L-AA, the main branches of the Ag structure became longer but were not abundant (Fig. 2c). Through a systematic study by changing the concentration of AgNO$_3$ and L-AA, it was found that 0.5 mM AgNO$_3$ and 50 mM L-AA could produce highly-branched coral-like Ag mesostructures which had more abundant main and subordinate branches (Fig. 2d).

Typical TEM images of highly-branched coral-like Ag mesoparticle synthesized with 0.5 mM AgNO$_3$ and 50 mM L-AA are shown in Fig. 3. As is illustrated in Fig. 3a, the TEM characterization also shows that the particles are uniform in morphology and size. Fig. 3b reveals that the highly-branched Ag particles are composed of many main and subordinate branches. On each main branch, there are several subordinate branches. The length of the main branches ranges from about 450 to 760 nm and the diameter is about 100 nm. For the subordinate branches, the length ranges from 30 to 200 nm and the diameter ranges from 30 to 80 nm. Fig. 3c shows a higher magnification image which indicates that the branches grow close to one another on the particle surface. The average space between two branches is less than 20 nm. The SAED (selected-area electron diffraction) pattern in the inset of Fig. 3c obtained from the branches indicates the branch is a single crystal. The composition analysis (Fig. S1†) by energy dispersive X-ray spectroscopy shows that except for Si element resulting from the Si substrate, the composition of the red circle area in Fig. S1a† is only silver.
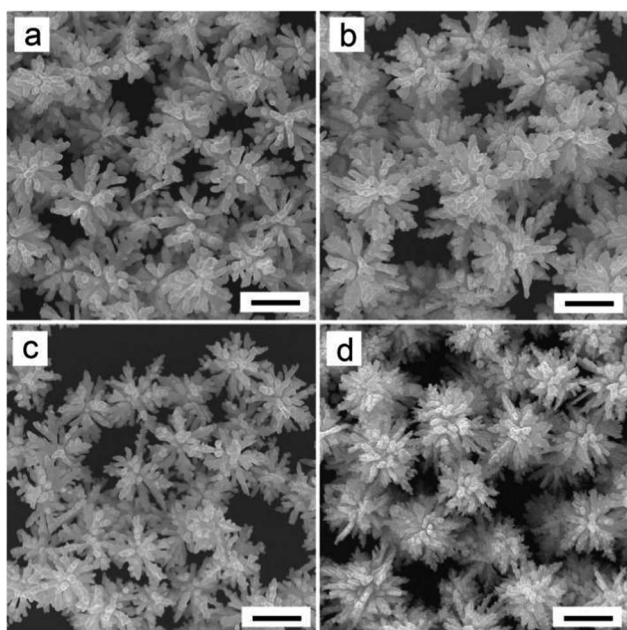

Fig. 2 SEM image of the products obtained with (a) 0.25 mM AgNO$_3$ and 0.5 mM L-AA, (b) 0.5 mM AgNO$_3$ and 1 mM L-AA, (c) 0.25 mM AgNO$_3$ and 10 mM L-AA, (d) 0.5 mM AgNO$_3$ and 50 mM L-AA. The reaction times were all 20 min. The scale bars represent 1 µm.

Mechanism of topography tuning

As we found in Fig. 1 and Table S1† under all the experimental conditions, the concentrations of AgNO$_3$ and L-AA have the most important effect on the morphology of the Ag mesoparticles.
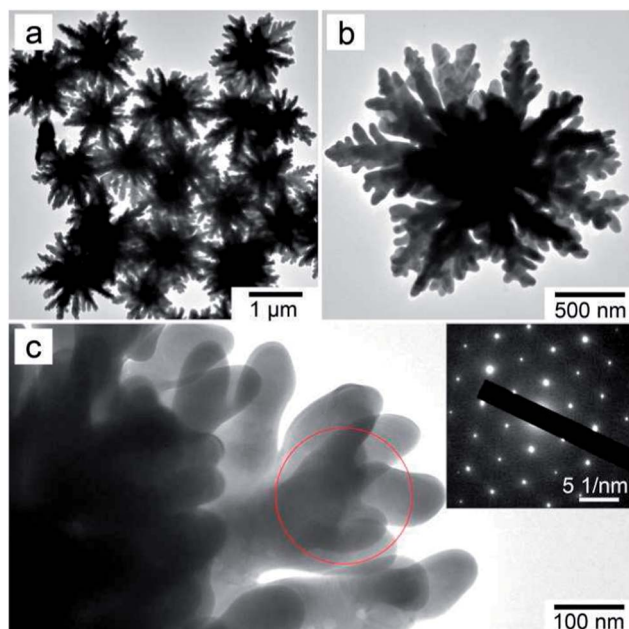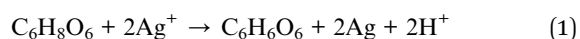
Fig. 3 TEM images of the highly-branched Ag mesoparticles. (a) TEM image of a large area of Ag mesoparticles. (b) TEM image of a single typical Ag mesoparticle. (c) High-magnification TEM image of the branches of the coral-like Ag mesoparticle. The inset in (c) shows the correlated SAED patterns from the circled area.
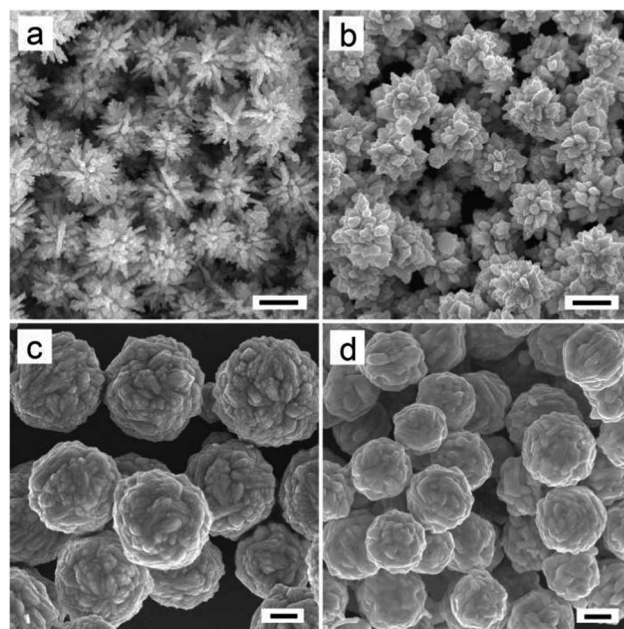

Fig. 4 SEM images of silver mesoparticles synthesized with 50 mM L-AA and different concentrations of $AgNO_3$: (a) 0.5 mM, (b) 1 mM, (c) 10 mM, and (d) 50 mM. The scale bars represent 1 μm.

The surface topography of the hierarchical Ag mesoparticles can be well tuned by changing the concentrations of $AgNO_3$ and L-AA. The topography tuning mechanism was studied and is discussed here. Fig. 4 shows that the morphology of the Ag particles can be tuned over a large range by only changing the concentration of $AgNO_3$ and keeping all the other conditions constant. When 50 mM L-AA was used and the $AgNO_3$ concentration was increased from 0.5 to 1, to 10 and to 50 mM, the morphology transformed from highly-branched hierarchical mesoparticles (Fig. 4a) to coral-like mesoparticles (Fig. 4b), and to meatball-like mesoparticles (Fig. 4c and d). A comparison of Fig. 4c and d shows that the size and surface roughness of the meatball-like particles can also be tuned to increase by changing the concentration of $AgNO_3$ from 50 to 10 mM.

The topography tuning mechanism of the hierarchical mesoparticles through changing the concentrations is illustrated in Fig. 5, using $AgNO_3$ concentration as an example. Xia's group has reported the transformation of the shape of Ag coral-like particles at different reaction times using SEM characterization.[32] The formation process of hierarchical Ag mesoparticles is similar to that of hierarchical Au mesoparticles reported in a previous study.[29,31,37] As shown in Fig. 5a, the formation process is a typical particle-mediated growth mode which can be divided into four stages.[38] In the first stage, the Ag^+ ions are reduced into Ag atoms by L-AA as follows:[39,40]

$$C_6H_8O_6 + 2Ag^+ \rightarrow C_6H_6O_6 + 2Ag + 2H^+ \qquad (1)$$

With the reaction proceeding, the concentration of Ag atoms in the solution gradually increases. The change in the
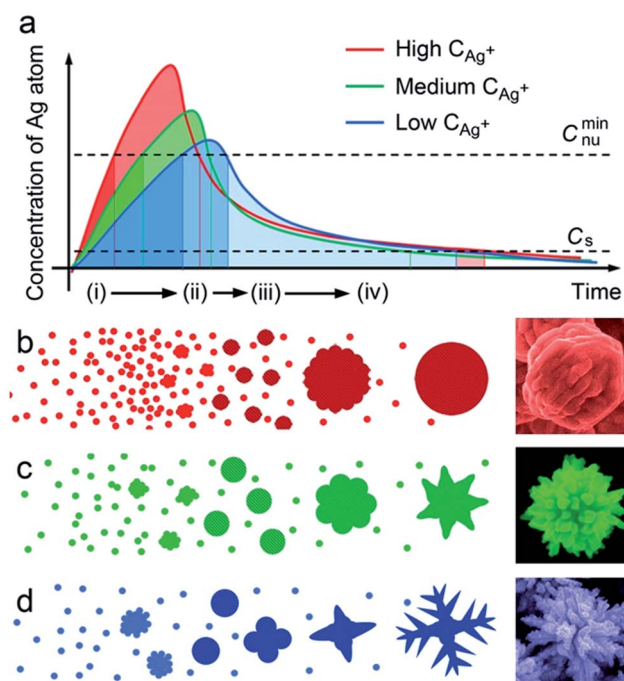
Fig. 5 Schematic illustration of the effect of Ag^+ concentration on the morphology of Ag mesoparticles. (a) The effect of Ag^+ concentration on the plot transformation of LaMer curves for the formation of Ag mesoparticles. (b–d) The formation process of various Ag mesoparticles with different Ag^+ concentration.

concentration of Ag atoms is schematically described using the LaMer curve in Fig. 5a. When the concentration of Ag atoms exceeds the supersaturation point of nucleation, the atoms aggregate to form a stable nucleus in the second stage. Thus, a

great number of Ag nanoparticles are formed in the solution. At the same time, the concentration of Ag atoms dramatically decreases accompanied by an increase in the concentration of Ag nanoparticles in the solution. When the concentration of Ag atoms decreases to below the supersaturation point of nucleation, the nanoparticles stop being produced. In this system, L-AA not only acts as a reducing agent, but also acts as a capping agent, which adsorbs on the particle surface for the stabilization of the nanoparticles. One L-AA molecule has four hydroxyl groups, so as with dopa molecules, the L-AA molecules promote the aggregation of Ag nanoparticles through their "glue" function.[29,31] In the third stage, the Ag nanoparticles aggregate to form spherical mesoparticles through a new and non-classical crystal growth, which is called "particle-mediated growth".[38,41] Through particle mediated growth, a polycrystalline or mesocrystal structure can be formed depending on the growth conditions.[42,43] The particle size of the Ag mesoparticles can be described by the following equation:

$$r = kT\rho^{2/3}/3\pi\eta f_m \qquad (2)$$

where, r is the radius of the mesoparticle, k is the Boltzmann constant, ρ and f_m are the density and suspending aggregation frequency of the nanoparticles, T and η are the temperature and viscosity of the solution. In this synthesis system, the solution is rotated with a magnetic bar, so T, ρ, and η are uniform in the whole solution, resulting in uniform distribution of mesoparticle size. In the fourth stage, the remaining Ag ions are reduced and deposited on the mesoparticles thus inducing overgrowth of the Ag mesoparticles. As with dopa molecules, the L-AA molecules also promote the tips of mesoparticles to preferentially overgrow, thus resulting in hierarchical morphology.

Usually, the chemical reaction rate increases as the reactant agent concentration increases. At high concentrations of Ag$^+$ ions, the reaction rate is quicker than that at medium and low concentrations. More Ag atoms are produced in the first and second stages (Fig. 5b). The higher supersaturation concentration of Ag atoms induces more and smaller nanoparticles in the second stage. These nanoparticles aggregate to form spherical mesoparticles under the "glue" function of L-AA. Because of the quick reaction at high concentrations, most of the Ag$^+$ ions are reduced to Ag atoms in the first three stages. Thus, in the last stage, there are not enough remaining Ag$^+$ ions for the mesoparticle overgrowth. Finally, only meatball-like mesoparticles are obtained. At medium and low concentrations of Ag$^+$ ions, the reaction rate becomes slow. A lower supersaturation concentration of Ag atoms occurs during the first two stages, which induces the formation of larger nanoparticles with a lower density (ρ) in the solution. Depending on eqn (2), smaller mesoparticles can be formed in the third stage. At the same time, more Ag$^+$ ions remain, which supports the overgrowth of the small protrusions. Thus, longer and sharper protrusions are formed in the fourth stage. Overall, as the concentration of Ag$^+$ ions decreases from high to low, the morphology of the mesoparticles transforms from meatball-like to coral-like, urchin-like, and even to highly-branched shapes.

Optical and SERS properties

The UV-Vis extinction spectra of Ag mesoparticles with different morphologies were measured and are shown in Fig. 6. The monodispersity of the mesoparticles allows the experimental observation of well-defined higher-order multipole plasmon modes in addition to the dipole resonance. The LSPR was determined by particle size and morphology.

With the protrusions on the mesoparticle surface becoming longer and sharper, the UV-Vis spectra peaks corresponding to higher-ordered multipole plasmon resonance modes in addition to the dipole resonance, such as quadrupole, octupole and hexadecapole, become clear and can be observed. For the meatball-like and coral-like mesoparticles (sample S1 and S3 in Fig. 6a and b), only one higher-order multipole, *i.e.* quadrupole, extinction peak can be found. For the urchin-like and highly-branched mesoparticles (sample S4 and S6 in Fig. 6c and d), two more higher-order multipoles, *i.e.* octopole and hexadecapole, appeared.

The SERS properties of Ag mesoparticles with tunable morphologies were evaluated by using crystal violet (CV), a well-known and commonly used SERS analyte. The SERS spectra of CV molecules adsorbed on individual Ag mesoparticles with four typical morphologies, sample S1, S3, S4, and S6 (as shown in Fig. 1), were measured using a confocal microprobe Raman spectrometer at an excitation wavelength of 633 nm as is shown in Fig. S2†. As the excitation wavelength of 633 nm lies within the absorption band of the resonance of CV molecules, the obtained Raman signal is due to belongs to the surface-enhanced resonance Raman scattering (SERRS). A fluorescent baseline is formed in the Raman spectra when the CV molecules are excited with a 633 nm laser as is shown in Fig. S4.† The obtained SERRS spectra in Fig. 7 reveal the characteristic peaks of CV, for instance, at 1172, 1371, 1619 cm^{-1}, and these correspond well to the ordinary Raman spectra of CV in the solid state and in aqueous solution.[44,45] An apparent trend of
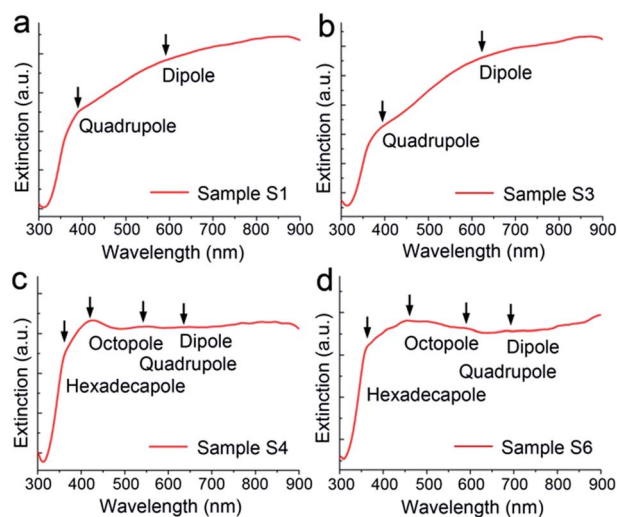

Fig. 6 UV-Vis spectra of Ag mesoparticles with different shapes, (a) S1: meatball-like, (b) S3: coral-like, (c) S4: urchin-like, and (d) S6: highly-branched morphologies.

4538 | *J. Mater. Chem. A*, 2014, **2**, 4534–4542

This journal is © The Royal Society of Chemistry 2014

increasing SERRS signal with an increase of surface texture is observed: the signal intensities for the 1172 cm^{-1} peak are found to increase by 1 : 5.1 : 6.2 : 13.9 for the mesoparticles of S1, S3, S4, and S6, respectively. Following the procedure and assumptions described in a previous report (details show in ESI†),[31] the EFs of SERS for CV molecules on mesoparticles S1, S3, S4, and S6, were estimated to be about 5.0×10^6, 1.3×10^7, 1.8×10^7, and 8.2×10^7, respectively. These results are consistent with previous reports, such as the estimated value of EFs $\sim 10^6$–10^7 for Au meatball-like mesoparticles and $\sim 10^7$ for Au urchin-like and Ag flower-like mesoparticles.[9,29,33] In this study, the EFs of the Ag meatball-like mesoparticles and urchin-like mesoparticle were 5.0×10^6, and 1.8×10^7, respectively.

Fig. 8 shows the SERRS spectra of CV molecules on particle aggregated films. A similar trend, the enhancement of single particles, was found for the particle aggregated film. The EFs for sample S1, S3, S4, and S6 were about 4.4×10^8, 8.7×10^8, 6.9×10^8, and 4.1×10^9, respectively. In the measurement, the laser spot was 850 nm in diameter and the particle size was about 1 to 2 μm. Thus, as shown in Fig. S3,† the detected area in the particle aggregated film was the border region between several particles. The aggregation of the hierarchical mesoparticles can greatly improve the enhancement of SERRS signals. This can be explained by the interparticle interactions in the particle aggregated film, which result in additional abundant "hot spots".[46] The Raman signal collection time was 20 s for single particle detection and 1 s for the detection of particle aggregated film. Comparing the signal intensities (1172 cm^{-1} peak) presented in Fig. 7 and 8, we estimated that the enhancements of the mesoparticle aggregated films were 88, 67, 38, and 50 times higher than that of the single particle for samples S1, S3, S4, and S6, respectively. As reported in previous work, the EF for urchin-like Au mesoparticle film exceeded the EF of the corresponding individual particle by 10–100 times, which is consistent with our results.[12]

Fig. 8 SERRS properties of Ag mesoparticle aggregated films. The films are made up of Ag mesoparticles of various shapes, S1: meatball-like, S3: coral-like, S4: urchin-like, and S6: highly-branched morphologies.

To corroborate the observed relationship between the SERS activity and the surface topography of the hierarchical Ag mesoparticles, we applied the three-dimensional FDTD method to calculate the local electromagnetic field intensity around the model particles irradiated with monochromatic light. Five model Ag mesoparticles were built and simulated using the FDTD method. They had different surface topographies, model A: spherical particles with a smooth surface, model B: meatball-like particles used to simulate sample S1, model C: coral-like particles used to simulate sample S3, model D: urchin-like particles used to simulate sample S4, and model E: highly-branched particles used to simulate sample S6. Their geometric parameters are shown in the ESI.†

Fig. 9a–k shows the typical distributions of the electric field E (plotted as color-code $\lg|E|^2$) calculated in a plane across a vertical axis of these model particles irradiated from the top by 633 nm light. It is generally agreed that the Raman intensity increases by a factor $|E|^4$ with respect to the local electric field on the SERS substrate surface.[47] The most localized and enhanced electromagnetic field areas (compared with the scale bars of the color code in Fig. 9) were found in the vicinity of the tips and gaps on the highly nanotextured mesoparticles surfaces. Comparing the electromagnetic field distribution maps for models A and B (Fig. 9a–d), it was found that the localized-electromagnetic field was excited by the nano-protrusions on the surface, as they act like nanolightning rods.[33,34] From a comparison of the enhanced localized-electromagnetic field in the vicinity of the nanoprotrusions of models B, C and D (Fig. 9c–h), we found that the longer and sharper protrusions on the surface can excite a stronger electromagnetic field on their tip surfaces (as indicated by arrows in Fig. 9d, f and h). Fig. 9f and h (as indication of arrows) revealing that an enhanced localized-electromagnetic field is also excited
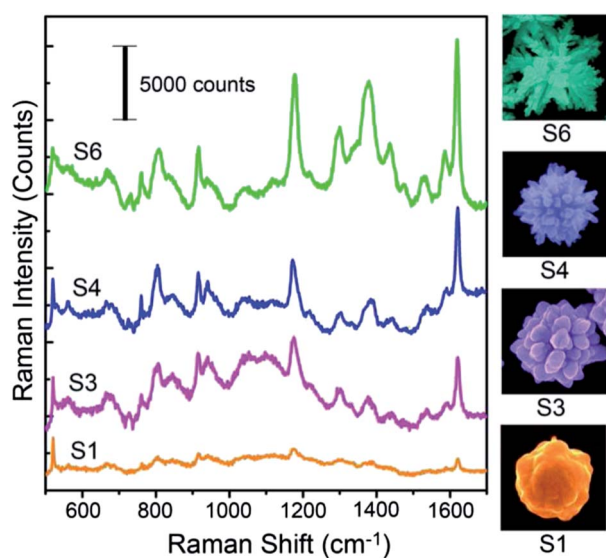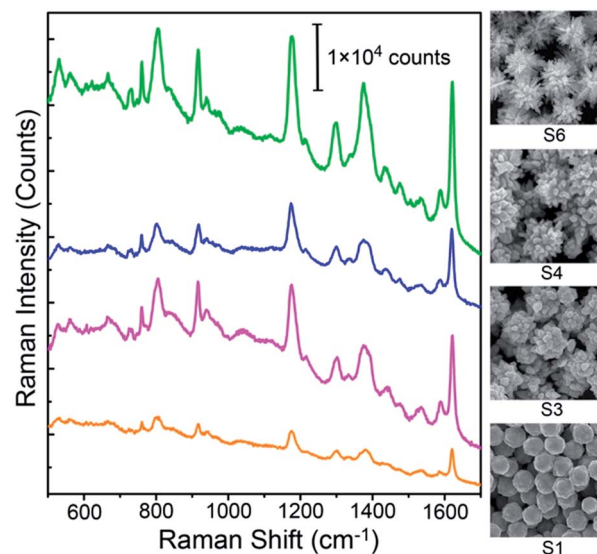

Fig. 7 Single-particle SERRS properties of Ag mesoparticles with different topographies, S1: meatball-like, S3: coral-like, S4: urchin-like, and S6: highly-branched morphologies.
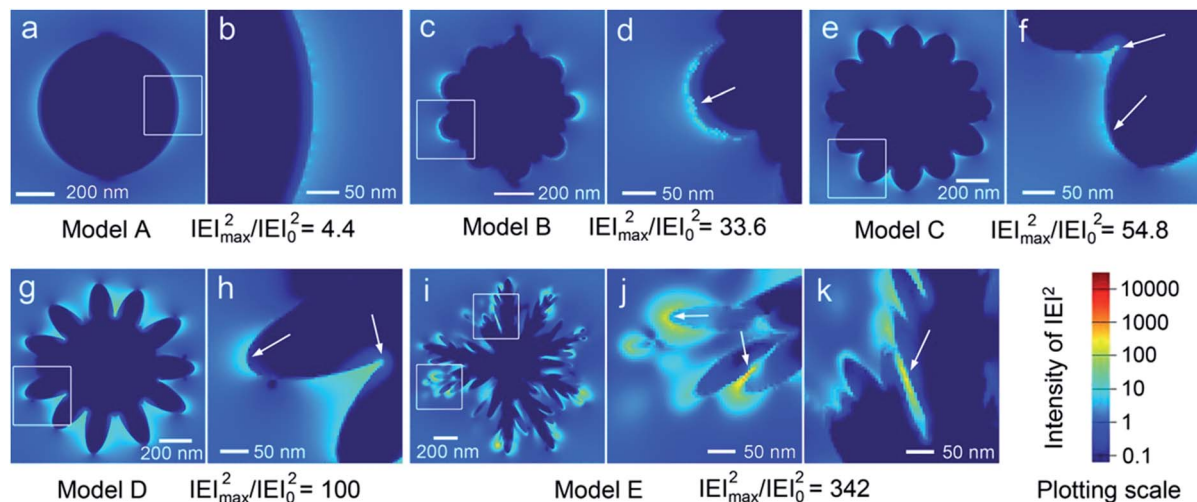
Fig. 9 The FDTD calculated electromagnetic field distribution and intensity of the individual Ag mesoparticles with various topographies under 633 nm incident laser, (a and b) model A: spherical mesoparticles, (c and d) model B: meatball-like mesoparticles, (e and f) model C: coral-like mesoparticles, (g and h) model D: urchin-like mesoparticles, and (i–k) model E: highly-branched mesoparticles. (b, d, f, h, j, k) Zoomed images from the circled areas.

in the gap formed between two protrusions. This can be explained by the fact that the exciting light is confined in the cavity of the gaps and induces a stronger SPR. Deeper and narrower gaps can more effectively confine the light in their cavity, resulting in stronger localized-electromagnetic field. Compared with coral-like and urchin-like mesoparticles, the highly branched mesoparticles have the sharpest protrusions and the narrowest gaps on their surface. At the same time, the densities of the protrusions and gaps are highest on the highly branched mesoparticles surfaces. Correspondingly, the number and intensity of SERS "hot spots" are largest on the surface of highly branched mesoparticles, as shown in Fig. 9i–k. So, highly branched nanotextured topographies are clearly favoured as the one potentially demonstrating the largest SERS enhancement (proportional to $\sim|E|^4$), in agreement with the experimental data.

Additionally, our FDTD simulation reveals that the excitation light wavelength also has an effect on the intensity of the localized-electromagnetic field. Fig. 10 displays the histograms of the maximal electromagnetic field intensity calculated from models A–E at excitation wavelengths of 514, 633, and 785 nm in x–y plane. These results indicate that the effect of the excitation wavelength on the electromagnetic field is highly dependent on the textured topographies of the mesoparticles. If the excitation light wavelength matches the SPR of the metal nanostructure, a stronger localized-electromagnetic field will be excited in the vicinity of the nanoprotrusions and nanogaps. Compared to models A to D, the highly branched Ag mesoparticles have an inhomogeneous surface texture and are therefore likely to exhibit broadened SPRs. Taking this into account, our FDTD simulations indicate that the optimal SERS excitation wavelength for highly branched mesoparticles would lie in the red and near-infrared spectral region, such as 633 and 785 nm, as shown in Fig. 10.

The extreme limit of single-particle SERS *versus* analyte concentration was evaluated using highly-branched Ag

mesoparticles. Quite dilute CV aqueous solutions with concentrations from 1.0×10^{-9} to 1.0×10^{-12} M were used here. As is shown in Fig. 11, when the CV concentration decreases to 1.0×10^{-11} M, the spectral features close to the characteristic vibrational peaks of CV (1172, 1371, 1619 cm^{-1}) can still be easily identified. When the CV concentration decreases even to 1.0×10^{-12} M, some feature peaks (such as 1371 and 1619 cm^{-1}) can still be identified. Previous studies showed that the extreme limits for the concentration of Ag mesoparticles with a rough surface were 1.0×10^{-11} and 1.0×10^{-12} M using CV solution.[23,48] So, in this study, the single-particle highly-branched Ag mesoparticles also show outstanding properties for the extreme concentration limit.
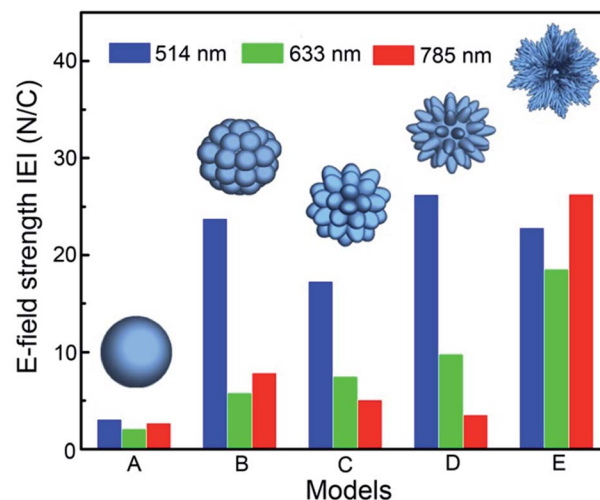

Fig. 10 Histograms of maximal electromagnetic field enhancements calculated from models A–E under excitation wavelengths of 514, 633, and 785 nm at x–y plane using FDTD calculation method.

4540 | J. Mater. Chem. A, 2014, 2, 4534–4542

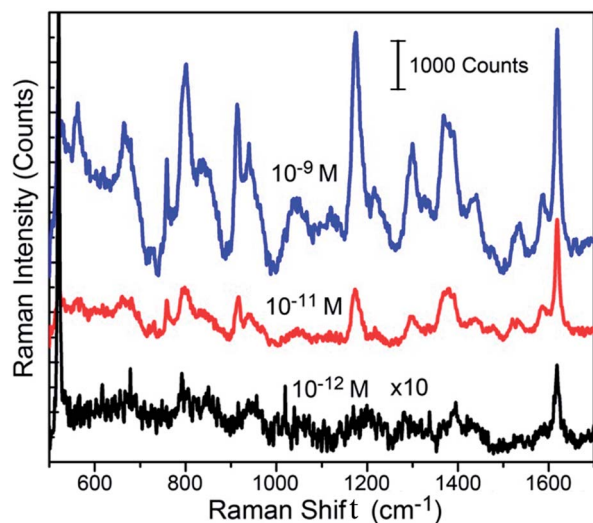This journal is © The Royal Society of Chemistry 2014

Fig. 11 Single-particle SERS spectra of CV molecules adsorbed on separated individual highly-branched Ag mesoparticles at decreased CV concentrations from 10^{-9} M to 10^{-11} M and 10^{-12} M.

Conclusions

In summary, hierarchical Ag mesoparticles with various surface morphologies have been synthetized in a simple and green synthesis system. In this reaction system, $AgNO_3$ is only reduced by L-AA at room temperature without the addition of any other capping agents and organics. The surface topographies of the mesoparticles can be well tuned by changing the concentrations of $AgNO_3$ and L-AA. In this particle-mediated growth system, lower concentrations will promote the anisotropic growth to form denser and sharper protrusions on the mesoparticle surface, which can greatly increase the SERS enhancement. The SERS EF of the arrayed highly branched Ag mesoparticles reaches more than 10^9. The FDTD simulation revealed that dense "hot spots" with the highest electromagnetic field were formed at the vicinity of the tips and gaps between protrusions by the excited SPR under the irradiation of monochromatic light. This study will help to understand the relationship between topography and SERS properties.

Acknowledgements

Notes and references

1 A. Campion and P. Kambhampati, *Chem. Soc. Rev.*, 1998, **27**, 241.
2 S. E. J. Bell and N. M. S. Sirimuthu, *Chem. Soc. Rev.*, 2008, **37**, 1012.
3 J. F. Li, Y. F. Huang, Y. Ding, Z. L. Yang, S. B. Li, X. S. Zhou, F. R. Fan, W. Zhang, Z. Y. Zhou, D. Y. Wu, B. Ren, Z. L. Wang and Z. Q. Tian, *Nature*, 2010, **464**, 392.
4 S. D. Hudson and G. Chumanov, *Anal. Bioanal. Chem.*, 2009, **394**, 679.
5 X. M. Wu, C. Xu, R. A. Tripp, Y. W. Huang and Y. P. Zhao, *Analyst*, 2013, **138**, 3005.
6 D. P. Cowcher, Y. Xu and R. Goodacre, *Anal. Chem.*, 2013, **85**, 3297.
7 Y. H. Zhao, W. Q. Luo, P. Kanda, H. W. Cheng, Y. Y. Chen, S. P. Wang and S. Y. Huan, *Talanta*, 2013, **113**, 7.
8 S. Gajaraj, C. Fan, M. S. Lin and Z. Q. Hu, *Environ. Monit. Assess.*, 2012, **185**, 5673.
9 H. Wang and N. J. Halas, *Adv. Mater.*, 2008, **20**, 820.
10 C. F. Tian, C. H. Ding, S. Y. Liu, S. C. Yang, X. P. Song, B. J. Ding, Z. Y. Li and J. X. Fang, *ACS Nano*, 2011, **5**, 9442.
11 M. F. Zhang, A. W. Zhao, H. H. Sun, H. Y. Guo, D. P. Wang, D. Li, Z. B. Gan and W. Y. Tao, *J. Mater. Chem.*, 2011, **21**, 18817.
12 J. X. Fang, S. Y. Du, S. Lebedkin, Z. Y. Li, R. Kruk, M. Kappes and H. Hahn, *Nano Lett.*, 2010, **10**, 5006.
13 M. Fleischm., P. J. Hendra and A. J. McQuilla, *Chem. Phys. Lett.*, 1974, **26**, 163.
14 M. Moskovits, *Rev. Mod. Phys.*, 1985, **57**, 783.
15 J. Bellessa, C. Symonds, K. Vynck, A. Lemaitre, A. Brioude, L. Beaur, J. C. Plenet, P. Viste, D. Felbacq, E. Cambril and P. Valvin, *Phys. Rev. B: Condens. Matter Mater. Phys.*, 2009, **80**.
16 W. Wu, G. Y. Jung, D. L. Olynick, J. Straznicky, Z. Li, X. Li, D. A. A. Ohlberg, Y. Chen, S. Y. Wang, J. A. Liddle, W. M. Tong and R. S. Williams, *Appl. Phys. A: Mater. Sci. Process.*, 2005, **80**, 1173.
17 Y. J. Chun, S. Nakajima and M. Kawabe, *Jpn. J. Appl. Phys.*, 1996, **35**, L1075.
18 S. Sakamoto, L. Philippe, M. Bechelany, J. Michler, H. Asoh and S. Ono, *Nanotechnology*, 2008, **19**, 405304.
19 X. Wen, G. Li, J. Zhang, Q. Zhang, B. Peng, L. M. Wong, S. Wang and Q. Xiong, *Nanoscale*, 2014, **6**, 132.
20 C. Cao, J. Zhang, X. Wen, S. L. Dodson, N. T. Dao, L. M. Wong, S. Wang, S. Li, A. T. Phan and Q. Xiong, *ACS Nano*, 2013, **7**, 7583.
21 S. Dodson, M. Haggui, R. Bachelot, J. Plain, S. Li and Q. Xiong, *J. Phys. Chem. Lett.*, 2013, **4**, 496.
22 J. M. Nam, D. K. Lim, K. S. Jeon, J. H. Hwang, H. Kim, S. Kwon and Y. D. Suh, *Nat. Nanotechnol.*, 2011, **6**, 452.
23 Z. Yang, L. Zhang, H. You, Z. Li and J. Fang, *Part. Part. Syst. Charact.*, 2013, DOI: 10.1002/ppsc.201300290.

24 B. Peng, G. Li, D. Li, S. Dodson, Q. Zhang, J. Zhang, Y. H. Lee, H. V. Demir, X. Yi Ling and Q. Xiong, *ACS Nano*, 2013, **7**, 5993.

25 X. M. Qian, X. H. Peng, D. O. Ansari, Q. Yin-Goen, G. Z. Chen, D. M. Shin, L. Yang, A. N. Young, M. D. Wang and S. M. Nie, *Nat. Biotechnol.*, 2007, **26**, 83.

26 L. Rodríguez-Lorenzo, R. n. A. Álvarez-Puebla, I. Pastoriza-Santos, S. Mazzucco, O. Stéphan, M. Kociak, L. M. Liz-Marzn and F. J. García de Abajo, *J. Am. Chem. Soc.*, 2009, **131**, 4616.

27 E. Nalbant Esenturk and A. R. Hight Walker, *J. Raman Spectrosc.*, 2009, **40**, 86.

28 H. X. Xu, E. J. Bjerneld, M. Kall and L. Borjesson, *Phys. Rev. Lett.*, 1999, **83**, 4357.

29 H. J. You, Y. T. Ji, L. Wang, S. C. Yang, Z. M. Yang, J. X. Fang, X. P. Song and B. J. Ding, *J. Mater. Chem.*, 2012, **22**, 1998.

30 M. J. Mulvihill, X. Y. Ling, J. Henzie and P. D. Yang, *J. Am. Chem. Soc.*, 2010, **132**, 268.

31 Z. Liu, F. Zhang, Z. Yang, H. You, C. Tian, Z. Li and J. Fang, *J. Mater. Chem. C*, 2013, **1**, 5567.

32 Y. Wang, P. H. C. Camargo, S. E. Skrabalak, H. Gu and Y. Xia, *Langmuir*, 2008, **24**, 12042.

33 H. Y. Liang, Z. P. Li, W. Z. Wang, Y. S. Wu and H. X. Xu, *Adv. Mater.*, 2009, **21**, 4614.

34 L. M. Tong, Z. P. Li, T. Zhu, H. X. Xu and Z. F. Liu, *J. Phys. Chem. C*, 2008, **112**, 7119.

35 F. Hao, C. L. Nehl, J. H. Hafner and P. Nordlander, *Nano Lett.*, 2007, **7**, 729.

36 H. You, C. Ding, X. Song, B. Ding and J. Fang, *CrystEngComm*, 2011, **13**, 4491.

37 J. P. Xie, Q. B. Zhang, J. Y. Lee and D. I. C. Wang, *ACS Nano*, 2008, **2**, 2473.

38 H. You, S. Yang, B. Ding and H. Yang, *Chem. Soc. Rev.*, 2013, **42**, 2880.

39 K. P. Velikov, G. E. Zegers and A. van Blaaderen, *Langmuir*, 2003, **19**, 1384.

40 L. Lu, A. Kobayashi, K. Tawa and Y. Ozaki, *Chem. Mater.*, 2006, **18**, 4894.

41 Z. M. Peng, H. J. You and H. Yang, *ACS Nano*, 2010, **4**, 1501.

42 J. Fang, B. Ding and H. Gleiter, *Chem. Soc. Rev.*, 2011, **40**, 5347.

43 J. X. Fang, H. J. You, P. Kong, Y. Yi, X. P. Song and B. J. Ding, *Cryst. Growth Des.*, 2007, **7**, 864.

44 X. M. Qian and S. M. Nie, *Chem. Soc. Rev.*, 2008, **37**, 912.

45 K. Kneipp, Y. Wang, H. Kneipp, L. T. Perelman, I. Itzkan, R. Dasari and M. S. Feld, *Phys. Rev. Lett.*, 1997, **78**, 1667.

46 J. P. Xie, J. Y. Lee and D. I. C. Wang, *Chem. Mater.*, 2007, **19**, 2823.

47 P. Dawson, J. A. Duenas, M. G. Boyle, M. D. Doherty, S. E. J. Bell, A. M. Kern, O. J. F. Martin, A. S. Teh, K. B. K. Teo and W. I. Milne, *Nano Lett.*, 2011, **11**, 365.

48 J. X. Fang, S. Y. Liu and Z. Y. Li, *Biomaterials*, 2011, **32**, 4877.